Palaeogeography, Palaeoclimatology, Palaeoecology 666 (2025) 112833

Contents lists available at ScienceDirect

Palaeogeography, Palaeoclimatology, Palaeoecology

journal homepage: www.elsevier.com/locate/palaeo

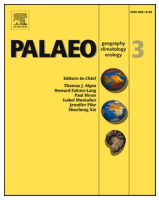

# Quantitative reconstruction of Holocene hydroclimate changes in northeastern China and implications for East Asian monsoon dynamics

Shi-Yong Yu *, Runzhe Xu

*Key Laboratory of Regional Sustainable Development System Analysis and Simulation in Higher Education Institutions, School of Geography, Geomatics, and Planning, Jiangsu Normal University, Xuzhou, China*

ARTICLE INFO

Editor: Pradeep Srivastava

*Keywords:*
Holocene climate variability
Hydroclimate reconstruction
East Asian monsoon
Data-model fusion
Atmospheric circulation shifts

ABSTRACT

The pattern of Holocene climate change remains unclear due to unresolved issues such as the "temperature conundrum" and the uncertain relationship between temperature and precipitation, particularly in monsoonal regions. Variability in regional climate drivers, including changes in ice volume, atmospheric circulation, and monsoon dynamics, further complicates Holocene climate dynamics, leading to spatially and temporally heterogeneous climate responses. As a result, reconstructing the precise timing, magnitude, and drivers of Holocene climate change remains challenging, requiring more detailed data and advanced statistical methods. In this study, we present a quantitative reconstruction of Holocene hydroclimate changes in northeastern China through a data-model fusion approach. By integrating water chemistry data from ostracod shells in a closed-basin lake with a hydrological balance model, we estimate growing-season temperature anomalies and relative lake-level changes during the Holocene. Our results highlight a mid-Holocene hydrological peak corresponding to the Holocene Thermal Maximum in the region. This peak lagged behind the early-Holocene summer insolation maximum, likely due to the influence of remnant ice sheets in the Northern Hemisphere. A comparison of our relative lake-level record with data of regional pollen-based precipitation reconstructions and TraCE-21 k modeling reveals a consistent pattern of increased monsoonal rainfall during the middle Holocene, followed by a steady decline after 5 kyr BP, reflecting a weakening of the East Asian summer monsoon. Additionally, our EOF analyses identify an early-Holocene tripolar precipitation pattern, which reversed in the middle Holocene, driven by shifts in atmospheric circulation. These findings advance our understanding of Holocene climate variability and offer insights for future climate predictions in monsoonal regions.

## 1. Introduction

Quantitative palaeoclimate reconstructions from chemical and biological proxies are indispensable for advancing climate science and supporting evidence-based policy (Tingley et al., 2012). One of the key benefits of quantitative palaeoclimate reconstruction is their ability to offer detailed climate records extending far beyond the instrumental period (Tierney et al., 2020). This long-term perspective not only enable us to identify patterns and regional climate anomalies, but also help us contextualize current climate trends and project future changes more accurately (Lunt et al., 2024). In addition, quantitative palaeoclimate reconstructions are fundamental for validating and refining climate models, ultimately enhancing their predictive capabilities. Moreover, these reconstructions are essential for assessing the impact of past climate changes on ecosystems, biodiversity, and human societies (Pfister, 2010). This knowledge is critical for developing strategies to mitigate and adapt to future climate challenges, ensuring that policies are informed by a deep understanding of climate dynamics.

The transfer function method is a widely-used statistical approach in palaeoclimatology for quantifying past climate conditions from proxy records (Kumke et al., 2004). It establishes an empirical relationship between modern climate variables (e.g., temperature and precipitation) and corresponding proxy data, allowing past climate changes to be inferred quantitatively. However, one limitation of this method is that it does not explicitly account for the underlying processes by which proxy records are formed. Another caveat is that proxies are often influenced by a variety of environmental factors, and the assumption that the same relationships between climate and proxies in the present hold true in the past may not always be valid (Guiot et al., 2000). Changes in boundary conditions, such as shifts in ocean circulation, atmospheric composition,

* Corresponding author.
*E-mail address:* syu@jsnu.edu.cn (S.-Y. Yu).

https://doi.org/10.1016/j.palaeo.2025.112833
Received 13 November 2024; Received in revised form 15 January 2025; Accepted 19 February 2025
Available online 23 February 2025

or land surface processes, can alter the relationship between proxies and climate variables, making the transfer function method less reliable for deep-time reconstructions particularly when environmental conditions differ significantly from those used to calibrate the transfer function.

Conceptually different from the transfer function method, proxy inverse modeling is a process-based approach to quantitative palaeoclimate reconstructions that infers past climate conditions by reversing the relationship between climate and proxy data (Guiot et al., 2009; Yu et al., 2012). It accounts for the physical, chemical, or biological mechanisms that govern proxy formation, offering a more accurate and mechanistic way to reconstruct past climates (Evans et al., 2013). By simulating how climate variables such as temperature and precipitation affect proxies, inverse modeling retrieves the most likely past climate states from proxy data (Yu, 2013). This approach offers several advantages over traditional statistical methods. First, it accounts for nonlinearities and uncertainties in the climate-proxy relationship, allowing for a more accurate and nuanced reconstruction of past climate conditions. Second, it can be applied across a wide range of time scales, from recent centuries to deep-time geological periods, making it highly versatile. Although computationally intensive and requiring detailed process knowledge (Dee et al., 2018), proxy inverse modeling significantly improves the precision of palaeoclimate reconstructions and informs more reliable future climate projections.

The Hydrologic Balance Inversion Model (HyBIM) is a simplistic inverse modeling framework designed to quantify relative changes in lake chemistry through a system of total differential equations (Ibarra and Chamberlain, 2015). These equations help to solve for key hydroclimate variables like temperature and lake volume using relative changes rather than relying on the absolute values of isotopic and trace element measurements. This feature allows the model to focus on trends and gradients rather than the full magnitude of changes. In this study, we reconstruct Holocene hydroclimate changes in northeastern China through a proxy inverse modeling approach. Lying at the juncture of monsoon and westerly-dominated climatic regimes, this region is highly susceptible to climate change and shifts in atmospheric circulation patterns (Zhao and Yu, 2012). By integrating stable oxygen isotope and trace element data of ostracod shells derived from Lake Hulun with HyBIM, quantitative information about growing-season temperature and lake-level anomalies relative to the present-day conditions are obtained. Our results show a trend of progressive cooling accompanied by steady lake-level fall following the Holocene Thermal Maximum, implying complex forcing and feedback mechanisms underlying hydroclimate changes in the margin of the East Asian monsoon domain.

## 2. Data and methods

### 2.1. Study area and site description

Lake Hulun (48°58′23″N, 117°26′08″E, 543 m asl), also known as Dalai Lake, ranks as the fifth largest lake in China, situated in the Inner Mongolia Autonomous Region, near the borders of China, Russia, and Mongolia (Fig. 1). The lake basin resides within the mid- to high-latitude zone (46–54°N, 108–124°E), at an elevation ranging from 400 to 700 m asl. The basin is bordered by the Kent Mountain range to the west and the Greater Khingan Mountains to the east, resulting in a diverse landscape of plains, grasslands, and forests. This region serves as a critical ecological barrier in North China, providing essential habitats for a variety of species. The climate is characterized as temperate continental (Xu et al., 1989), influenced by the complex interactions between East Asian monsoons and the westerlies. The mean annual temperature is approximately 0.3 °C, with July being the hottest month, averaging 20.3 °C, while January experiences the coldest temperatures, averaging −21.2 °C. Annual precipitation totals around 352 mm, with the majority (80 %) occurring during the summer months (June to August). However, the region faces significant evaporation, with rates reaching approximately 1411 mm annually, creating unique hydrological and climatic conditions.

Hulun Lake, encompassing an area of 2339 km$^2$, and Buir Lake,

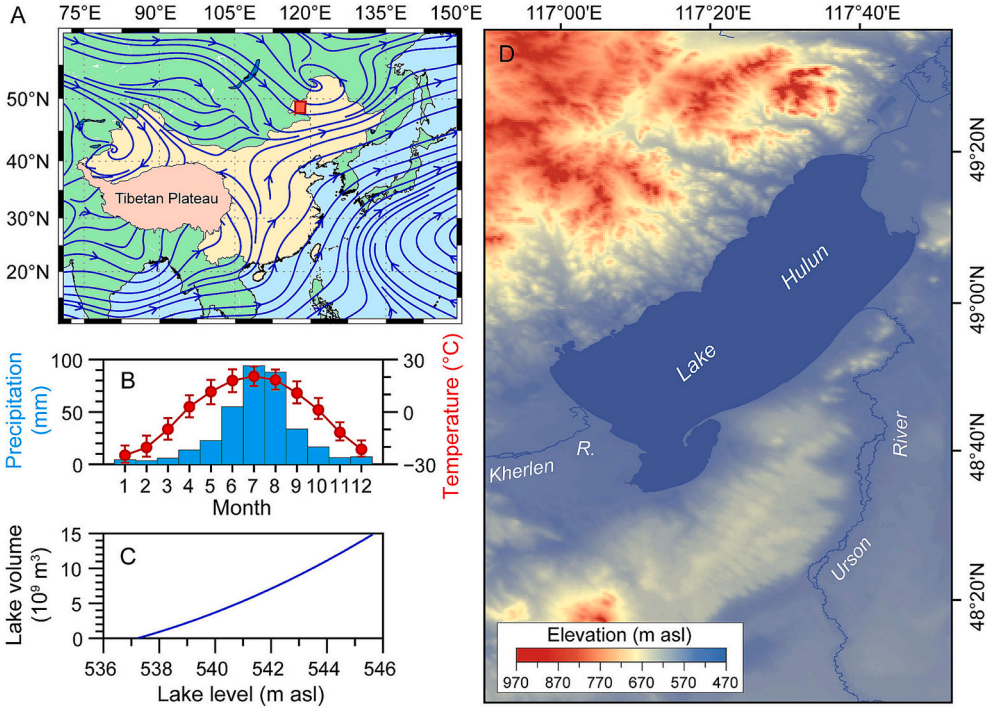


**Fig. 1.** Map showing the physical setting of Lake Hulun. (A) Regional atmospheric circulation patterns during summer. Stream field was created using June–July-August mean 850-hPa winds of NCEP Reanalysis products (1981–2010). Red box denotes Lake Hulun. (B) Seasonal variation in precipitation and temperature, (C) Relationship between lake level and lake volume (Ma et al., 2022), and (D) Topographical context and the surrounding drainage system. (For interpretation of the references to colour in this figure legend, the reader is referred to the web version of this article.)

covering 609 km$^2$, are the major water bodies within the basin, although many smaller lakes remain hydrologically disconnected from the river systems. Geologically, the basin is underpinned by the complex structure of the Greater Khingan Mountains fold belt and the Mesozoic rift basin (Xu et al., 1989), formed along the suture zone between the North China and Siberian plates. This area predominantly features Cenozoic sandstones, along with older Jurassic and Ordovician strata comprising tuffs, sandstones, rhyolites, and various granite and volcanic intrusions. Groundwater sources primarily consist of bedrock fissure aquifers within these geological formations, while Quaternary sand and gravel deposits sustain pore water aquifers in the downstream plains, playing a crucial role in maintaining the regional hydrological system. Lake Hulun itself extends over 93 km in length, with a maximum width of 41 km. Its average depth is 5.7 m, with a maximum depth of 8 m, holding a water volume of approximately 13.85 × 10$^9$ m$^3$. The lake is primarily replenished by the Kherlen River, originating in Mongolia, and the Urson River, which connects Buir Lake to Lake Hulun.

Lake Hulun is classified as a slightly saline lake, with a pH of 9.2 and a salinity of 2.5 g/L (Zhai et al., 2011; Wu et al., 2015). The ranking of cation equivalent concentrations is $Na^+ > Mg^{2+} > K^+ > Ca^{2+}$, with sodium being the dominant cation, accounting for 76.6 % of the total cation molar concentration. For anions, the order of equivalent concentrations is $Cl^- > SO_4^{2-} > HCO_3^-$, with chloride and sulfate as the predominant anions, representing 49.6 % and 29.3 % of the total anion molar concentration, respectively. The hydrochemical type of the lake water is classified as $Cl^-{\cdot}SO_4^{2-}$-$Na^+$ (Wu et al., 2015). The molar ratios of Mg/Ca and Sr/Ca of the lake water are 8.8 and 0.02 (Zhai et al., 2011; Wu et al., 2015), respectively.

### 2.2. Water chemical data and preprocessing

The ostracod species currently inhabiting Lake Hulun include *Limnocythere inopinata* (Baird), *Candoniella suzini* Schneider, *Pseudocandona albicans* (Brady), *Pseudocandona compressa* (Koch), *Cyclocypris serena* (Koch), *Ilyocypris gibba* (Ramdohr), and *Ilyocypris salebrosa* Stepanaiths (Xu et al., 1989). Among these, *L. inopinata* is the dominant species over the last 11,000 years (Zhai et al., 2011). The water chemical data used to infer past hydroclimate conditions include $\delta^{18}O$, molar ratios of Sr/Ca and Mg/Ca, which were measured on the valves of adult L. *inopinata* ostracods extracted from the HL06 core sediments. The chronological framework of this core is constrained by 13 radiocarbon ages (Zhai et al., 2011). These data collectively reveal significant hydrological and chemical changes in Lake Hulun over the Holocene (Fig. 2). Specifically, the $\delta^{18}O$ values likely track changes in the mean annual temperature and water balance of the lake, while the Sr/Ca and Mg/Ca ratios indicate shifts in lake water chemistry associated with water balance. The marked fluctuations in these records reflect regional hydroclimate responses to monsoon strength, evaporation rates, or inflow variations, providing insights into past environmental conditions in the lake and its catchment.

According to the requirements of HyBIM (Ibarra and Chamberlain, 2015), all data should be smoothed and interpolated into an evenly spaced time series. We employ the Epanechnikov kernel function to smooth the data because of its finite boundaries compared to the Gaussian kernel function. To avoid over- or under-smoothing, optimal bandwidth selection for each time series was performed by minimizing the mean sum squares using 10-fold cross-validation, resulting in bandwidths of 212, 208, and 232 years for the $\delta^{18}O$, Sr/Ca, and Mg/Ca records, respectively. The smoothed time series were then interpolated linearly to a 100-year resolution, which is much longer than the water residence time of the lake (around 6 years). To deal with the uncertainty inherent in the data, the standard error was constructed for each smoothed time series by calculating the residuals and counting the number of data points within the bandwidth. These uncertainties, along with the smoothed and interpolated dataset, will be input to the subsequent Monte Carlo routine.

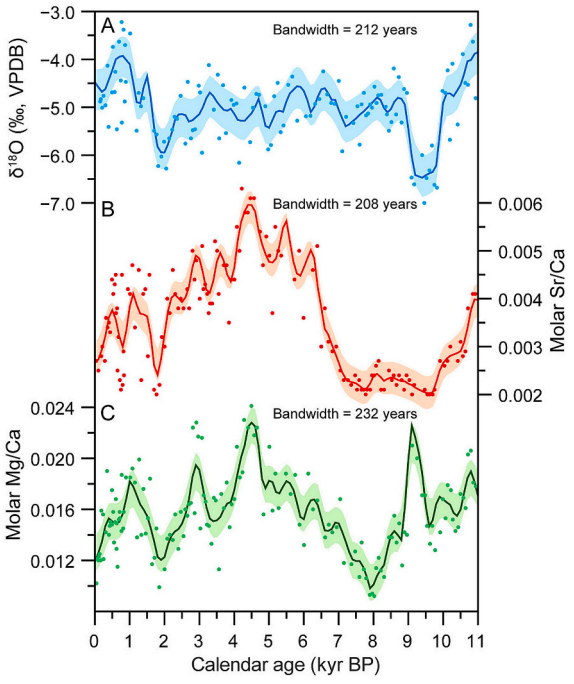


**Fig. 2.** Water chemical records used to infer hydroclimate changes in the Lake Hulun basin. (A) Stable oxygen isotope, (B) Molar ratio of Sr/Ca, and (C) Molar ratio of Mg/Ca. Shaded area denotes the 2σ uncertainties.

HyBIM also requires that all of the input data should be placed in terms of isotopic and trace elemental composition of the lake water (Ibarra and Chamberlain, 2015). The $\delta^{18}O$ record derived from ostracod shells is subject to both the vital effect and the temperature effect. According to sediment trap studies in Lake Qinghai (Li and Jin, 2013), the vital effect of L. *inopinata*, defined as the difference of the $\delta^{18}O$ values between ostracod shells and fine-grained authigenic carbonate, is 1.34 ± 0.68 ‰ (Table 1). We subtract this value from the $\delta^{18}O$ values of ostracod shells and then convert them to the V-SMOW scale. We calculate the equilibrium fractionation factor, $\alpha_{eq}$, derived from the equation by Kim and O'Neil (Kim and O'Neil, 1997)

$$\alpha_{eq} = exp\left(\frac{18.03 \times 10^3/T - 32.42}{1000}\right) \quad (1)$$

where $T$ is water temperature in Kelvin. With this factor, the $\delta^{18}O$ values

**Table 1**
Parameters used for the HyBIM model in this study.

| Parameter | Description | Value | References |
|---|---|---|---|
| $\varepsilon_v$ | $\delta^{18}O$ vital effect of *Limnocythere inopinata* | 1.34 ± 0.68 ‰ | (Li and Jin, 2013) |
| $T$ | Hypolimnetic temperature | 0 ± 2 °C | (Xu et al., 1989) |
| $h$ | Relative humidity | 60 ± 10 % | (Xu et al., 1989) |
| $k_D[Sr^{2+}]$ | Molar distribution coefficient of Sr/Ca | 0.62 ± 0.02 | (Zhang et al., 2004) |
| $k_D[Mg^{2+}]$ | Molar distribution coefficient of Mg/Ca | 9.68 × 10$^{-5}$ × $T$ ± 0.16 × 10$^{-5}$ | (Engstrom and Nelson, 1991) |
| $[Ca^{2+}]_l$ | Molar $Ca^{2+}$ concentration in lake water | 183.1 ± 70.6 μmol/L | (Wu et al., 2015) |
| $[Sr^{2+}]_s$ | Molar $Sr^{2+}$ concentration in source water | 2.76 ± 0.61 μmol/L | (Jin et al., 2010) |
| $[Mg^{2+}]_s$ | Molar $Mg^{2+}$ concentration in source water | 780.5 ± 41.1 μmol/L | (Han et al., 2018) |
| $[\delta^{18}O]_s$ | Weighted mean $\delta^{18}O$ of source water | −10.14 ± 1.24 ‰ | (Liang et al., 2017) |

of lake water, $[\delta^{18}O]_l$, can be reconstructed from

$$[\delta^{18}O]_l = \frac{1000 + [\delta^{18}O]_o}{\alpha_{eq}} \quad (2)$$

where $[\delta^{18}O]_o$ is the $\delta^{18}O$ values of ostracod shells in the V-SMOW scale. Converting the molar ratio of Sr/Ca and Mg/Ca of ostracod shells to that of lake water is straightforward. This is done by dividing them by their distribution coefficients. According to modern studies in Lake Qinghai (Zhang et al., 2004), a distribution coefficient of 0.62 ± 0.02 was used for the Sr/Ca ratios of L. *inopinata*. However, for the Mg/Ca ratios of many species, the distribution coefficient has been shown to be temperature-dependent (Engstrom and Nelson, 1991). We reconstruct the ion concentrations of these trace elements in lake water by multiplying the Sr/Ca and Mg/Ca ratios of lake water by the concentration of $Ca^{2+}$ (181.3 ± 70.6 μmol/L) in modern lake water (Table 1).

### 2.3. Description of HyBIM and algorithm

HyBIM is an inverse model designed to analyze changes in lake water chemistry by solving a system of total differential equations (Ibarra and Chamberlain, 2015), which helps deduce the relative changes in temperature and lake volume. Unlike models that rely on absolute values, HyBIM utilizes first-order difference to approximate the first derivative of input datasets, making it especially useful for studying relative changes in hydroclimatic conditions. Building on previous qualitative models that used end-member mixing techniques to interpret lacustrine deposits, HyBIM draws upon the covariance of geochemical markers such as $\delta^{18}O$, Sr/Ca, and Mg/Ca, especially suited for closed-basin lakes where evaporation and hydrologic inputs dominate. To account for uncertainty in the data and model parameters, a Monte Carlo routine is applied.

HyBIM follows a structure similar to those used to examine the global carbon cycle and other biogeochemical cycles, as developed in works by Goddéris and others (Goddéris and François, 1996; François and Goddéris, 1998), and is constrained by total differential equations. These are the backbone of the model, allowing for the inversion and solving of extensive variables like temperature, hydrologic input, and evaporation. We made a slight improvement to the model by expressing a partial derivative of geochemical markers in terms of changes in the source, which are further connected to changes in climate (Appendices). Let $\mathbf{y} = ([\delta^{18}O]_l, [Sr^{2+}]_l, [Mg^{2+}]_l)'$ denote a vector of concentration of these geochemical markers and $\mathbf{x} = (T, F_i, F_e)'$ denote a vector of hydroclimate variables, with $T$ being growing-season temperature, $F_i$ being the fractional increase of lake volume due to external input, and $F_e$ being the fractional decrease of lake volume due to evaporative loss, where the prime symbol denotes the transpose of a vector. Using the chain rule of differentiation, changes in lake water chemistry, $d\mathbf{y}$, associated with changes in hydroclimate variables, $d\mathbf{x}$, can be expressed as

$$\begin{pmatrix} d[\delta^{18}O]_l \\ d[Sr^{2+}]_l \\ d[Mg^{2+}]_l \end{pmatrix} = \begin{pmatrix} \frac{\partial[\delta^{18}O]_l}{\partial[\delta^{18}O]_p}\frac{\partial[\delta^{18}O]_p}{\partial T} & \frac{\partial[\delta^{18}O]_l}{\partial F_i} & \frac{\partial[\delta^{18}O]_l}{\partial F_e} \\ \frac{\partial[Sr^{2+}]_l}{\partial[Sr^{2+}]_s}\frac{\partial[Sr^{2+}]_s}{\partial T} & \frac{\partial[Sr^{2+}]_l}{\partial F_i} & \frac{\partial[Sr^{2+}]_l}{\partial F_e} \\ \frac{\partial[Mg^{2+}]_l}{\partial[Mg^{2+}]_s}\frac{\partial[Mg^{2+}]_s}{\partial T} & \frac{\partial[Mg^{2+}]_l}{\partial F_i} & \frac{\partial[Mg^{2+}]_l}{\partial F_e} \end{pmatrix} \times \begin{pmatrix} dT \\ dF_i \\ dF_e \end{pmatrix} \quad (3)$$

Let $\mathbf{A}$ denote the Jacobian matrix in the above equation, with each item being defined in the Appendices. Changes in the hydroclimate variables, say $d\mathbf{x}$, in each timestep can be obtained from

$$d\mathbf{x} = \mathbf{A}^{-1} d\mathbf{y} \quad (4)$$

where $\mathbf{A}^{-1}$ is the inverse of matrix $\mathbf{A}$, and $d\mathbf{y}$ can be approximated by the first-order difference of the geochemical markers. As HyBIM made a linearization on the Jacobian matrix with a proscribed value of 1.1 for $F_i$ and 0.1 for $F_e$ (Ibarra and Chamberlain, 2015), drastic, order-of-magnitude fluctuations in lake volume are unable to handle. We relax this limitation by retaining the nonlinear form of matrix $\mathbf{A}$ and solving for $\mathbf{x}$ through a data-driven optimization. Specifically, we take the backward difference of the input time series from the present to the past and use the present-day (1961–2009 CE) hydroclimatic condition as the initial value, denoted as $\mathbf{x}_0$, to find a tentative solution for $\mathbf{x}$ at the end of the first timestep by integrating Eq. 4 backward using the Euler method. We then perturb $\mathbf{x}$ iteratively until the mean square error between the data and the predictions become reasonably small such that

$$\hat{\mathbf{x}} = \underset{\mathbf{x}}{argmin}((d\mathbf{y} - \mathbf{A}(\mathbf{x}) \bullet (\mathbf{x} - \mathbf{x_0}))'(d\mathbf{y} - \mathbf{A}(\mathbf{x}) \bullet (\mathbf{x} - \mathbf{x_0}))). \quad (5)$$

We use $\mathbf{x}$ as the initial value for the next timestep and repeat this procedure for all the remaining timesteps to find a series of optimal solutions for the hydroclimate variables. Changes in growing-season temperature relative to the present-day condition, say $\Delta T$, can be obtained from

$$\Delta T_k = f(x) = \begin{cases} 0, & k = 0 \\ \sum_{j=1}^{k} (T_{j+1} - T_j), & k = 1, \cdots, N-1 \end{cases} \quad (6)$$

where $N$ is the number of data points in each time series. Similarly, changes in lake volume with respect to the present-day conditions, say $\Delta V$, can be obtained from

$$\Delta V_k = \begin{cases} 0, & k = 0 \\ \sum_{j=1}^{k} \left( \left[ (F_i)_{j+1} - (F_i)_j \right] - \left[ (F_e)_{j+1} - (F_e)_j \right] \right) - 1, & k = 1, \cdots, N-1 \end{cases} \quad (7)$$

## 3. Results

The reconstructed changes in growing-season temperature and lake volume anomalies with respect to the present-day (1951–2010 CE) conditions are presented in Fig. 3, with mean estimates and uncertainty ranges derived from 5000 Monte Carlo simulations. The results indicate that early-Holocene growing-season temperatures were similar to those of the present day, followed by a sharp decline around 9 kyr BP and a subsequent recovery. Temperatures continued to rise, reaching a peak along with maximum lake volume during the middle Holocene, before

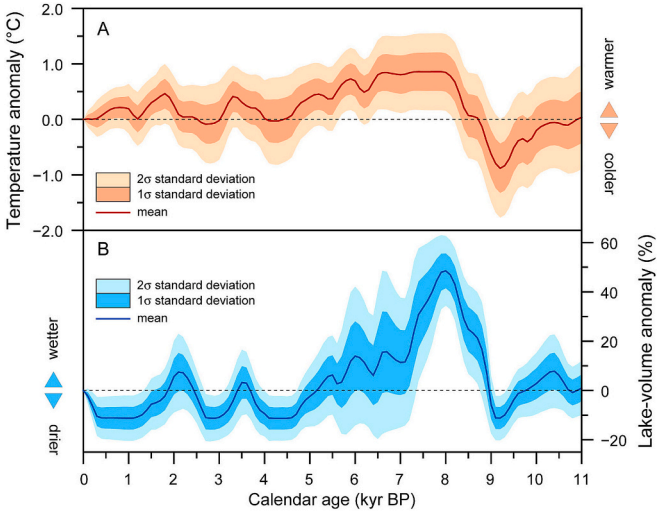


**Fig. 3.** Inferred Holocene hydroclimate changes relative to present-day conditions in the Lake Hulun basin. (A) Mean annual temperature, and (B) Lake volume.

cooling and a corresponding reduction in lake volume during the late Holocene. Notably, the inferred growing-season temperature fluctuated, with the most significant warming occurring between 8 and 6 kyr BP, followed by gradual cooling. This trend reflects multiple phases of moderate warming and cooling (<1 °C), but overall stability closes to present-day levels throughout the Holocene.

Our results demonstrate a strong, significant correlation ($r = 0.6$, $p < 0.001$) between temperature and lake volume dynamics at Lake Hulun, indicating a consistent pattern of hydroclimate changes over an extended period. For instance, lake volume dropped sharply around 9 kyr BP, followed by a peak between 9 and 7 kyr BP, coinciding with temperature changes. The subsequent decreases in both temperature and lake volume suggest a shift to cooler, potentially drier conditions, which may have contributed to declining lake levels. These fluctuations highlight the complex interplay between temperature and hydrological processes in the region during the Holocene. Overall, the pattern suggests that periods of climatic warming were associated with increased lake volume, while cooling phases resulted in lower water levels. The inverse relationship observed over the last 1000 years appears to be an artifact, likely resulting from the application of different bandwidths in data smoothing. This evidence aligns with broader Holocene climate trends, where temperature and hydrological shifts were driven by natural variations in solar radiation and atmospheric circulation patterns.

## 4. Discussion

### 4.1. Temporal and spatial complexity of Holocene temperature changes

Understanding the trend of postglacial temperature changes is crucial not only for interpreting Holocene climate dynamics but also for assessing the context of current warming trend, as the warmth observed in recent decades might have few precedents within the Holocene. Our results indicate that climate conditions in the Lake Hulun basin were cooler than today between 11 and 10 kyr BP. This cooler period was followed by a gradual warming trend, peaking between 8 and 6 kyr BP, when growing-season temperatures reached their highest value, approximately 1 °C warmer than today. This magnitude of warming supports for a relatively mild millennial-scale global thermal maximum during the mid-Holocene (Kaufman and Broadman, 2023). Our findings are also consistent with mid-to-high latitudinal (Marcott et al., 2013), Northern Hemispheric (Zhang et al., 2022), and global (Kaufman et al., 2020) reconstructions based on terrestrial proxy records (Fig. 4A), which show a warmer climate during the 8 to 6 kyr BP period, commonly referred to as the Holocene Thermal Maximum (HTM). While many of these records represent mean annual temperatures, the timing of the HTM is virtually identical for winter, summer, and annual temperature reconstructions (Cartapanis et al., 2022). After this thermal peak, mean growing-season temperatures began a gradual decline, though millennial-scale fluctuations occurred, especially in more recent millennia. Over the last few thousand years, growing-season temperatures in the region stabilized closer to today's levels, showing relatively stable conditions with only modest variability.

In contrast to the widely recognized long-term cooling after the HTM, recent paleoclimate reconstructions (Bova et al., 2021) and paleoclimate assimilations (Osman et al., 2021) based on marine proxy data show a more continuous warming trend up until the industrial era (Fig. 4B). This warming is consistent with General Circulation Model (GCM) simulations (Liu et al., 2014), which suggests a steady rise in global temperatures throughout the Holocene, driven by increasing greenhouse gas concentrations and orbital forcing (Fig. 4C). This divergence between proxy-based reconstructions and model simulations, referred to as the Holocene temperature conundrum, highlights the complexity of long-term climate dynamics and the need for integrated approaches to reconcile these differences. Simulations like TraCE-21 k, which rely solely on orbital and ice-volume forcings, can replicate the peak warmth of the middle Holocene followed by gradual

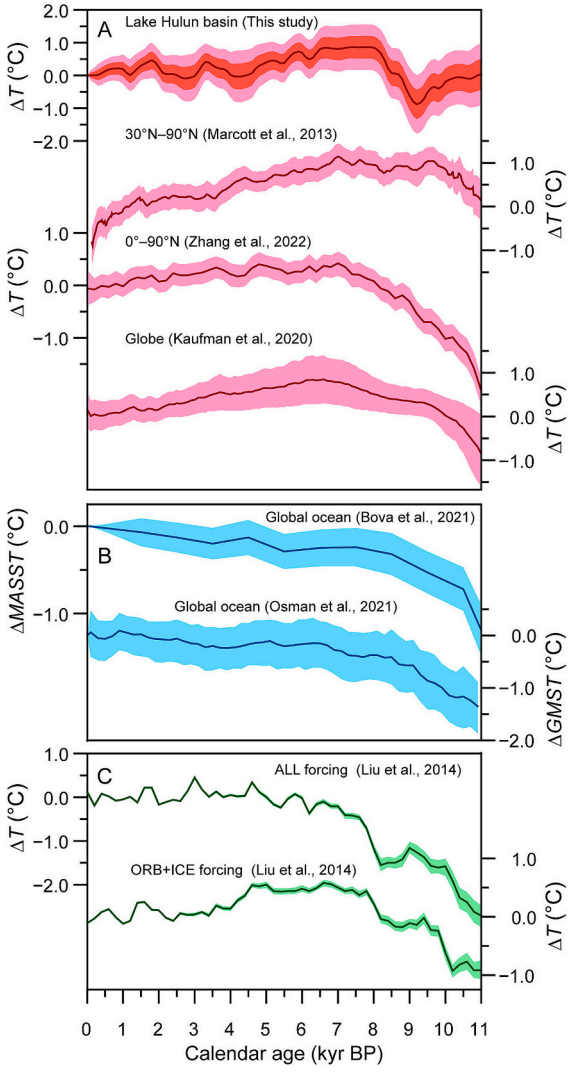


**Fig. 4.** Comparison of regional and global Holocene temperature records. (A) Growing-season temperature anomalies inferred from Lake Hulun (this study), middle-high latitudinal mean annual temperature anomalies (Marcott et al., 2013), Northern Hemispheric mean annual temperature anomalies (Zhang et al., 2022), and global mean annual temperature anomalies (Kaufman et al., 2020), (B) Mean annual sea-surface temperature (MASST) anomalies (Bova et al., 2021) and global mean surface temperature (GMST) anomalies (Osman et al., 2021), and (C) TraCE-21 k modeled Northern Hemispheric mean annual temperature anomalies (Liu et al., 2014).

cooling (Fig. 4C). However, they indicate that additional climate forcing and significant feedbacks are required to counteract the effects of greenhouse-gas forcing in current models. For example, incorporating early land-use changes into Holocene climate models significantly improves the agreement between models and proxy data (Hopcroft et al., 2023). Additionally, time-slice simulations from the Community Earth System Model suggest that the expansion of Northern Hemispheric vegetation around 9 and 6 kyr BP may have warmed Earth's surface by 0.8 °C and 0.7 °C, respectively, producing a better fit with proxy reconstructions (Thompson et al., 2022). A recent synthesis of winter temperature indices also emphasizes the HTM pattern (Jiang et al., 2024), suggesting that the seasonal bias hypothesis alone cannot fully resolve the model-data discrepancy. This work highlights that increased dust loading during the mid-to-late Holocene likely played a critical role in driving the post-HTM cooling trend and should be accounted for in models of Holocene temperature evolution.

The pattern of Holocene temperature changes exhibits notable

spatial complexity. Reconstructed temperatures from sub-fossil pollen across 642 sites in North America and Europe indicate an overall warming trend that aligns with model simulations, while a long-term cooling trend is confined to the North Atlantic region (Marsicek et al., 2018). Our results from the East Asian monsoon region, along with many continental proxy records from mid-to-high latitudes in the Northern Hemisphere (Fig. 4A), show a HTM between 8 and 6 kyr BP. In contrast, marine proxy records from the same latitudes suggest an earlier HTM, occurring between 11 and 7 kyr BP (Cartapanis et al., 2022), while the tropics lack a clear temperature anomaly (Bader et al., 2020). These findings suggest a heterogeneous response to orbital forcing, emphasizing the absence of a globally synchronous HTM. New statistical approaches, such as proxy-system models and data assimilation techniques, may significantly reduce uncertainty in proxy-based reconstructions. Using empirical orthogonal function (EOF) analyses of outputs from the HadCM3 and TraCE-21 k simulations, combined with the Temp-12 k proxy database, which includes 1319 temperature-sensitive proxy records from 679 global locations (Erb et al., 2022), we highlight the spatiotemporal complexity of Holocene temperature changes (Fig. 5). Our results (Fig. 5A) align with the HTM mode (Fig. 5B), which accounts for approximately 83 % of global temperature anomalies, while the warming mode (Fig. 5C) contributes minimally (around 9 %) to these anomalies. Moreover, the spatial EOF modes indicate that the cooling trend predominantly occurs across the Eurasian landmass and the North Atlantic region (Fig. 5D), while the warming trend is concentrated between 20°N and 90°S (Fig. 5E).

### 4.2. *Holocene relative lake-level changes linked to East Asian monsoon dynamics*

The proximity of Lake Hulun to the Siberian high-pressure system and westerlies suggests that the region is influenced by both continental and monsoonal climate dynamics (Fig. 1A), contributing to its distinct seasonal climate pattern, with a wet and warm summer followed by a cold and dry winter (Fig. 1B). Therefore, the lake volume is highly responsive to changes in precipitation controlled by these larger atmospheric circulation systems. Moreover, Lake Hulun is situated in a low-lying basin, where small increases in lake level can lead to substantial expansions in water volume (Fig. 1C), highlighting the sensitivity of the lake to hydrological and climatic changes. The strong seasonality in precipitation, combined with the lake's sensitivity to water-level changes, makes Lake Hulun an important site for studying past and present climate variability in the region. Based on the relationship between lake level and lake volume (Ma et al., 2022), we render the inferred relative lake-volume changes to lake-level fluctuations ($\Delta H$) with respect to the present-day levels (Fig. 6A). The lake level remained relatively low between 11 and 9 kyr BP, with slight fluctuations around −1 m. During the middle Holocene (9–5 kyr BP), the lake level began to rise significantly, approaching the outflow threshold (around 2.75 m above the current level) by about 7.5 kyr BP. Following the peak, there was a progressive decline in lake levels with fluctuations until around 2 kyr BP. In the most recent two millennia, the lake level remained relatively stable, oscillating close to the current level.

The relative lake level changes in the Hulun basin reflect broader hydroclimatic shifts during the Holocene (Zhao and Yu, 2012). To understand the driving mechanisms behind these changes, we compiled pollen-based annual precipitation records from closed-basin lakes located in the margins of the East Asian monsoon domain (Fig. 6B-E) and TraCE-21 k simulations (Fig. 6F). These records consistently indicate reduced precipitation during the early Holocene, corresponding to a generally dry period with limited hydrological input into the lake. For example, the Lake Bayanchagan record reveals a relatively arid climate, with annual precipitation around 400 mm (Jiang et al., 2006). Similarly, the Chagan Nur record from the southern Mongolian Plateau reflects a semi-arid environment, with annual precipitation ranging between 325 and 375 mm (Li et al., 2020). The Lake Daihai record also indicates a predominantly semi-arid climate, with annual precipitation 50–100 mm lower than present (Xu et al., 2010). Meanwhile, Lake Gonghai, situated at the margin of the East Asian summer monsoon area, shows slightly reduced annual precipitation during this period (Chen et al., 2015). All precipitation curves show a peak during the middle Holocene, which corresponds to the HTM, a period associated with increased monsoon intensity. This aligns with the high lake levels, indicating wetter conditions in the region and a significant hydrological input into the lake basin during this time. It is noteworthy that reconstructed lake-level histories in Lakes Chagan Nur (Li et al., 2020), Dali (Jiang et al., 2020), and Daihai (Goldsmith et al., 2022) show highstand during the early-to-middle Holocene. This prolonged high lake-level status is likely due to potential dating uncertainties. After 5 kyr BP, there was a consistent decline in precipitation across all curves, corresponding to a decrease in lake levels. This marks a transition to drier conditions, which could be linked to weakening monsoonal activity during the late

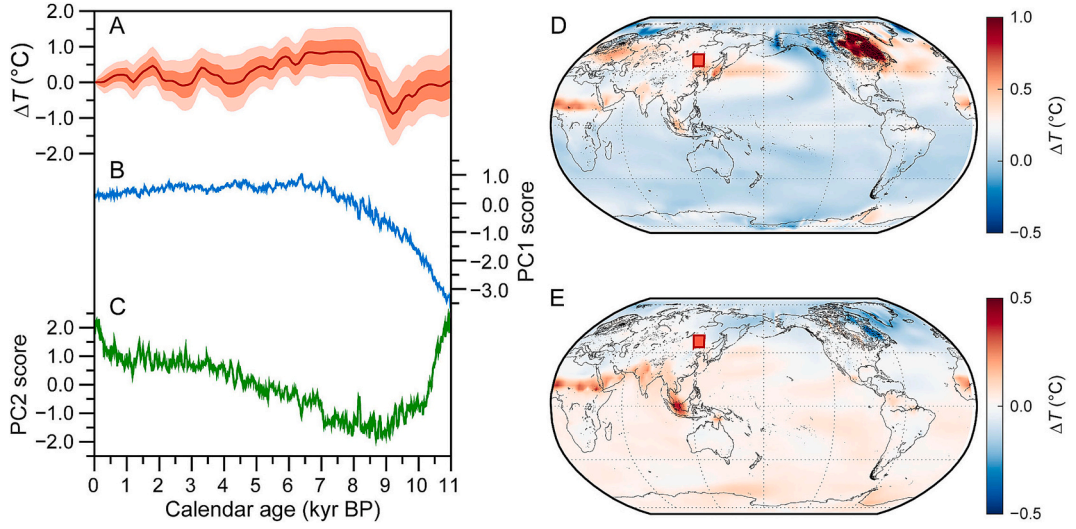


**Fig. 5.** Comparison of Holocene temperature record from Lake Hulun with paleoclimatic data assimilation. (A) Growing-season temperature anomalies inferred from Lake Hulun (this study), (B) First principal component (PC1) of global mean annual temperature anomalies, (C) Second principal component (PC2) of global mean annual temperature anomalies, (D) First empirical orthogonal function (EOF1) mode of global mean annual temperature anomalies, and (D) Second empirical orthogonal function (EOF2) mode of global mean annual temperature anomalies. Filled square denotes Lake Hulun.

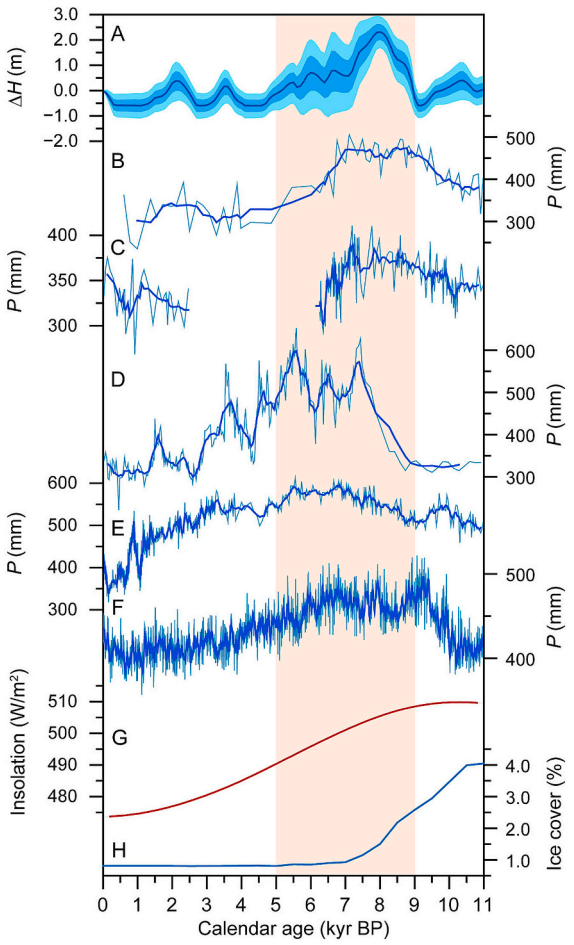


**Fig. 6.** Comparison of Holocene relative lake-level changes in Lake Hulun with pollen-based and modeled annual precipitation in northern China. (A) Lake Hulun (this study), (B) Lake Bayanchagan (Jiang et al., 2006), (C) Chagan Nur (Li et al., 2020), (D) Lake Daihai (Xu et al., 2010), (E) Lake Gonghai (Chen et al., 2015), (F) TraCE-21 k simulations over 100–120°E, 40–50°N (He and Clark, 2022), (G) 60°N summer insolation (Berger and Loutre, 1991), and (H) Areal-weighted Northern Hemispheric ice cover (Peltier et al., 2015). Vertical band highlights the peak of humidity in the margin of East Asian summer monsoon (Zhao and Yu, 2012).

Holocene. Superimposed on this trend are centennial-scale fluctuations in both lake levels and precipitation values, indicating variable summer monsoon activity.

Comparing the lake-level record with precipitation records reveals pervasive hydroclimatic changes throughout the Holocene, with a mid-Holocene lake-level highstand corresponding to the warmest and wettest climate. Notably, this hydroclimate peak significantly lagged behind the maximum summer insolation in the high latitudes of the Northern Hemisphere during the early Holocene (Fig. 6G). The lagged response of hydroclimate relative to insolation is a classic example of the complex interplay between external forcing and internal Earth system processes. Alongside higher summer insolation levels during the early Holocene, large ice sheets in North America and Scandinavia were still present prior to 7 kyr BP (Fig. 6H). These remnant ice sheets played a critical role in driving early-Holocene hydroclimatic patterns (Renssen et al., 2009), which moderated the effects of increased insolation by not only reflecting solar radiation but also absorbing substantial amounts of heat for melting and maintaining cooler temperatures. Also, the melting of these ice sheets is a gradual process, releasing significant volumes of freshwater into the North Atlantic, which disrupted the Atlantic Meridional Overturning Circulation. This influx of freshwater likely reduced the efficiency of heat transport from tropical regions to higher latitudes, further dampening regional warming and delaying the onset of the hydroclimate peak. As the ice sheets continued to recede, this buffering effect decreases, allowing temperatures to rise more rapidly into the middle Holocene. By this time, the diminished ice volume allowed for a stronger monsoon system and a more direct response to the higher levels of insolation (Jin et al., 2014), thereby resulting in the hydroclimate peak and maximum lake levels. Other factors, such as oceanic thermal inertia, increasing greenhouse gas concentrations and expanding vegetation cover, may have also contributed to this pattern (Chen et al., 2021).

The gradual melting of ice sheets and the associated impacts on ocean circulation and atmospheric patterns likely controlled the strength of the East Asian summer monsoon (Liu et al., 2015), which is sensitive to both temperature and oceanic conditions. The latitudinal displacement of the expansive Western Pacific Subtopic High (WPSH), with anticyclonic southeasterly winds manifesting as the East Asian summer monsoon (EASM), played a vital role in regulating regional hydrological cycle during the Holocene (Chen et al., 2021). To elucidate the driving mechanism behind the contrasting patterns of hydroclimatic changes between the early and middle Holocene, we conduct EOF analyses of annual precipitation simulated by the TraCE-21 k model over East Asia (He and Clark, 2022). The first EOF mode of annual precipitation anomalies during the early Holocene (11–9 kyr BP) reveals a distinct tripolar spatial structure (Fig. 7A). This pattern manifests as dry conditions in northern and southern China, flanking a wetter central region. The spatial distribution of these precipitation anomalies reflects the complex interplay between regional atmospheric circulation patterns and monsoonal dynamics, with the Mongolia High (MH) and the WPSH playing pivotal roles by inducing zones of moisture divergence and convergence, respectively. During the middle Holocene (8–6 kyr BP), the first EOF mode of annual precipitation anomalies retains a tripolar structure but exhibits an opposite phase (Fig. 7B). This phase reversal signifies a major climatic shift: the previously dry northern and southern regions became wetter, while the wet central region experienced reduced rainfall. These changes likely result from shifts in the strength and positioning of the key atmospheric systems, particularly the MH and the WPSH, alongside broader adjustments in the EASM. The persistence of the WPSH over central China led to drier conditions in the Yangtze River basin, while a northward shift of the Intertropical Convergence Zone (ITCZ) contributed to increased precipitation in southern China. Concurrently, enhanced precipitation in North China highlights a strengthened EASM.

While the underlying mechanisms driving the formation of this "mega-sandwich" pattern remain unclear (Chen et al., 2024), the shift in the tripolar hydroclimatic pattern from the early to middle Holocene was shaped by a complex interplay of orbital dynamics, atmospheric processes, and land surface interactions (Chen et al., 2021). Declining summer insolation during the middle Holocene weakened the EASM, limiting the northward penetration of rainfall and altering the spatial distribution of precipitation. Simultaneously, the retreat of Northern Hemisphere ice sheets caused a northward shift of the westerly jet stream, reducing its interaction with the EASM (Nagashima et al., 2013). The reduced influence of the westerlies over central China further disrupted moisture transport and contributed to the observed shift of the hydroclimatic regime (Herzschuh et al., 2019).

Changes in the strength and position of the WPSH also played a pivotal role (Shi et al., 2024). During the early Holocene, a weaker and equatorward-positioned WPSH facilitated moisture transport into central China. In contrast, a stronger and more westward-extending WPSH during the middle Holocene suppressed rainfall over central China while enhancing moisture delivery to northern and southern regions. Additionally, the northward displacement of the ITCZ, driven by global climatic adjustments, further amplified rainfall in southern China (Lu et al., 2024). Land-atmosphere feedbacks, including enhanced vegetation cover in northern China and reduced vegetation in central China (Chen et al., 2021), likely reinforced these precipitation patterns. These

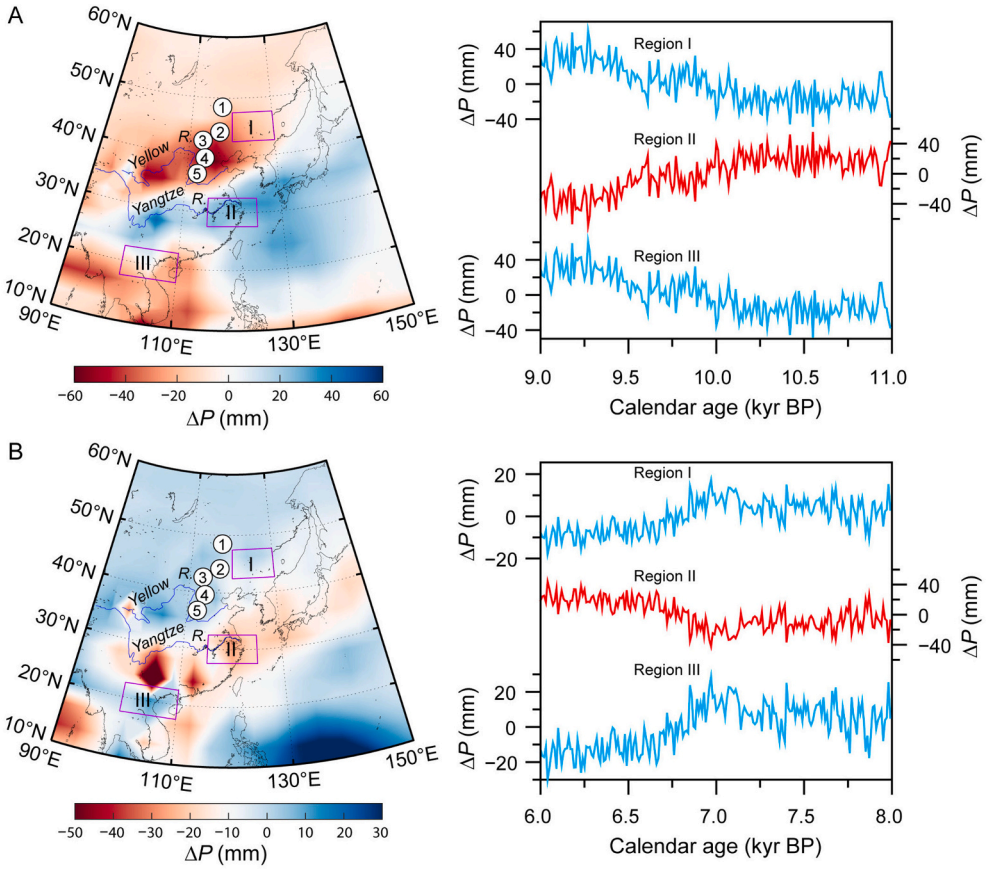


**Fig. 7.** Leading mode of annual precipitation variations over East Asia identified by the first empirical orthogonal function (EOF) analysis. (A) EOF1 spatial pattern (left panel) and associated precipitation anomalies ($\Delta P$) in three regions (right panel) during the early Holocene (11–9 kyr BP), (B) EOF1 spatial pattern (left panel) and associated precipitation anomalies ($\Delta P$) in three regions (right panel) during the middle Holocene (8–6 kyr BP). These two patterns explain 28 % and 22 % of the total variability, respectively. Analyses are based on the TraCE-21 k modeling dataset (He and Clark, 2022). Numbered dots denote sites mentioned in the text with 1 = Lake Hulun, 2 = Lake Bayanchagan, 3 = Chagan Nur, 4 = Lake Daihai, and 5 = Lake Gonghai, while numbered boxes represent regions used to calculate the area-weighted mean of EOF1 reconstructed precipitation anomalies with I = 120–130°E, 42.5–47.5°N, II = 115–125°E, 27.5–32.5°N, and III = 100–110°E, 17.5–22.5°N.

interwoven factors highlight the complexity of Holocene climate dynamics and the need for high-resolution data and modeling to disentangle their relative contributions.

## 5. Conclusions

We provide a detailed quantitative reconstruction of Holocene hydroclimate changes in the Lake Hulun basin, northeastern China, and offer insights into the spatial-temporal dynamics of climate evolution in the margin of the East Asian monsoon region. Key insights into the hydroclimatic evolution and monsoon dynamics can be summarized as follows:

(1) Our findings reveal a pronounced mid-Holocene hydrological peak corresponding to the HTM, which marks the warmest and wettest period in the basin. Notably, this hydroclimatic peak lagged behind the early Holocene maximum of summer insolation in the Northern Hemisphere, likely due to the moderating influence of remnant ice sheets in North America and Scandinavia.
(2) Comparing between inferred relative lake levels in the Lake Hulun basin and pollen-based precipitation records from surrounding regions demonstrates a consistent pattern of increased monsoonal precipitation during the middle Holocene, followed by a steady decline in rainfall after 5 kyr BP. This shift toward drier conditions is linked to a weakening of the EASM, which resulted in reduced hydrological input and falling lake levels during the late Holocene.
(3) The EOF analyses further reveal that the early Holocene was dominated by a tripolar precipitation pattern, with reduced rainfall in northern and southern China and enhanced moisture convergence in central China. This pattern was reversed in the middle Holocene, reflecting major shifts in regional atmospheric circulation, such as changes in the Mongolia High, the Western Pacific Subtropical High, and the ITCZ.
(4) Our study reveals the spatial heterogeneity and phased nature of Holocene hydroclimatic changes in the margin of the East Asian monsoon domain. The results highlight the importance of regional climate drivers, such as ice volume and monsoonal dynamics, in shaping the complex climate history of northeastern China. These findings contribute to a better understanding of past climate variability and its implications for future climate scenarios in monsoon-dominated regions.

## CRediT authorship contribution statement

**Shi-Yong Yu:** Writing – review & editing, Writing – original draft, Software, Methodology, Investigation, Formal analysis, Conceptualization. **Runzhe Xu:** Writing – review & editing, Data curation.

## Declaration of competing interest

The authors declare that they have no known competing financial

interests or personal relationships that could have appeared to influence the work reported in this paper.

## Data availability

Code is reposited in Zenodo with open access (https://zenodo.org/records/14641805).

## Acknowledgements

We thank the two anonymous reviewers for their constructive comments and suggestions, which have significantly improved the quality and clarity of our manuscript.

## Appendix A. Deriving the partial derivatives of $\delta^{18}O$ in lake water

Let $[\delta^{18}O]_l$ and $[\delta^{18}O]_p$ denote the $\delta^{18}O$ values of lake water and atmospheric precipitation, respectively. Define $F_i$ as the fractional increase in lake volume due to the input of source water and $F_e$ as the fractional decrease in lake volume due to evaporation, with $F_i > 1$ and $0 < F_e < 1$. Changes in the $\delta^{18}O$ values of lake water essentially involve three processes: (1) changes in the isotopic composition of precipitation, which is further related to regional climate; (2) changes in lake volume due to the input of source water, including atmospheric precipitation, river runoff, and groundwater discharge; and (3) changes in lake volume due to evaporative loss. Therefore, the total derivative of $[\delta^{18}O]_l$ can be expressed as

$$d\left[\delta^{18}O\right]_l = \frac{\partial[\delta^{18}O]_l}{\partial[\delta^{18}O]_p}\frac{\partial[\delta^{18}O]_p}{\partial T}dT + \frac{\partial[\delta^{18}O]_l}{\partial F_i}dF_i + \frac{\partial[\delta^{18}O]_l}{\partial F_e}dF_e \tag{A1}$$

Using isotopic data on atmospheric precipitation from the Qiqihar station (1988–1992) in the Global Network of Isotopes in Precipitation (GNIP), the local meteoric water line (LMWL) can be formulated as (Liang et al., 2017)

$$\delta D_p = 7.59\left[\delta^{18}O\right]_p - 0.03 \tag{A2}$$

Based on stable isotope analyses of water samples from the Hulun Lake, the evaporation line (EL) is given as (Ma et al., 2022)

$$\delta D_l = 4.80\left[\delta^{18}O\right]_l - 32.12 \tag{A3}$$

Equating the above two equations and differentiating $[\delta^{18}O]_l$ with respect to $[\delta^{18}O]_p$ yields $\frac{\partial[\delta^{18}O]_l}{\partial[\delta^{18}O]_p} = 1.5813$. In high latitudes, the isotopic composition of atmospheric precipitation is primarily influenced by the temperature effect (Dansgaard, 1964), with a slope $\frac{\partial[\delta^{18}O]_p}{\partial T} = 0.58$ per mil/°C (Rozanski et al., 1993).

Let $V_0$, $[\delta^{18}O]_0$, and $[\delta^{18}O]_s$ denote the initial value of lake volume, the initial $\delta^{18}O$ value of lake water, and the weighted $\delta^{18}O$ value of source water, respectively. Assuming isotopic mass conservation in the lake water and no isotopic fractionation from the input of source water, we have

$$\left[\delta^{18}O\right]_l F_i V_0 = \left[\delta^{18}O\right]_s (F_i - 1)V_0 + \left[\delta^{18}O\right]_0 V_0 \tag{A4}$$

Solving this equation for $[\delta^{18}O]_l$ yields

$$\left[\delta^{18}O\right]_l = \frac{[\delta^{18}O]_s(F_i - 1) + [\delta^{18}O]_0}{F_i} \tag{A5}$$

Differentiating Eq. A5 with respect to $F_i$ leads to

$$\frac{\partial[\delta^{18}O]_l}{\partial F_i} = \frac{[\delta^{18}O]_s - [\delta^{18}O]_0}{F_i^2} \tag{A6}$$

Unlike the input of isotopically light source water, which typically causes depletion of the heavy oxygen isotope ($\delta^{18}O$), evaporation generally leads to the enrichment of the heavy isotope due to fractionation. During evaporation, the heavy isotope becomes more concentrated as the lighter isotope is progressively removed from the lake water. To model oxygen isotopic fractionation in lake surface water, we use the modified Rayleigh equation for unsaturated open systems (Jouzel and Merlivat, 1984). Let $R_0$ denote the initial ratio of $^{18}O$ to $^{16}O$ in lake water. After the immediate removal of a fraction $F_e$ of lake water, the ratio of $^{18}O/^{16}O$ in the remaining lake water, denoted as $R_l$, is given by

$$R_l = R_0(1 - F_e)^{\alpha - 1} \tag{A7}$$

where $\alpha = \frac{1}{\alpha_e \alpha_k}$ represents the combined equilibrium and kinetic fractionation factors.

According to Horita and Wesolowski (1994), the equilibrium fractionation factor ($\alpha_e$) can be expressed as

$$\alpha_e = exp\left(\frac{0.35041 \times 10^6}{T^3} - \frac{1.6664 \times 10^3}{T^2} + \frac{6.7123}{T} - 7.685 \times 10^{-3}\right) \tag{A8}$$

where $T$ is the water temperature in Kelvin. According to Jouzel and Merlivat (1984), the kinetic fractionation factor ($\alpha_k$) during vapor formation under undersaturated conditions can be expressed as

$$\alpha_k = \left(\frac{1}{D}\right)^n (1 - h) + h \tag{A9}$$

Where $n = 0.5$ is the turbulent exponent and $D = 0.9723 \pm 0.0007$ is the ratio of diffusive transport of water molecules over an open water body under natural conditions (Pfahl and Wernli, 2009), and $h \in (0,1)$ is the relative humidity. Using the $\delta$ notation defined as $\delta_l = \left(\frac{R_l}{R_{std}} - 1\right) \times 1000$ per mil,

where $R_{std}$ is the $^{18}O/^{16}O$ ratio of the V-SMOW reference water, Eq. A7 can be reformulated as

$$\left[\delta^{18}O\right]_l = 1000\left(1+\left[\delta^{18}O\right]_0\right)(1-F_e)^{\alpha-1} - 1000 \tag{A10}$$

Differentiating this equation with respect to $F_e$ yields

$$\frac{\partial[\delta^{18}O]_l}{\partial F_e} = 1000(1-\alpha)\left(1+\left[\delta^{18}O\right]_0\right)(1-F_e)^{\alpha-2} \tag{A11}$$

## Appendix B. Deriving the partial derivatives of trace elements Sr and Mg

Let $M_l$ and $M_s$ denote the concentration of $Sr^{2+}$ or $Mg^{2+}$ in the lake water and source water, respectively. Similar to the $\delta^{18}O$ value, the total derivative of $M_l$ can be expressed as

$$dM_l = \frac{\partial M_l}{\partial M_s}\frac{\partial M_s}{\partial T}dT + \frac{\partial M_l}{\partial F_i}dF_i + \frac{\partial M_l}{\partial F_e}dF_e \tag{A12}$$

Let $M_0$ denote the initial concentration of a trace metal element ($Sr^{2+}$ or $Mg^{2+}$) in lake water. Assuming mass conservation, as trace metal elements are non-separable during the input of source water, we have

$$M_l F_i V_0 = M_s(F_i-1)V_0 + M_0 V_0 \tag{A13}$$

Solving this equation for $M_l$ leads to

$$M_l = \frac{M_s(F_i-1)+M_0}{F_i}. \tag{A14}$$

Differentiating Eq. A14 with respect to $M_s$ gives

$$\frac{\partial M_l}{\partial M_s} = 1 - \frac{1}{F_i} \tag{A15}$$

It appears that the concentration of trace metal elements in the source water is independent of climate. Thus, $\frac{\partial M_l}{\partial T} = 0$. Differentiating Eq. A14 with respect to $F_i$ results in

$$\frac{\partial M_l}{\partial F_i} = \frac{M_s - M_0}{F_i^2} \tag{A16}$$

Similarly, mass conservation of trace metal elements in lake water during evaporation yields

$$M_l(1-F_e)V_0 = M_0 V_0 \tag{A17}$$

Solving this equation for $M_l$ gives

$$M_l = \frac{M_0}{1-F_e} \tag{A18}$$

Differentiating this equation with respect to $F_e$ yields

$$\frac{\partial M_l}{\partial F_e} = \frac{M_0}{(1-F_e)^2} \tag{A19}$$

## References


Bader, J., Jungclaus, J., Krivova, N., Lorenz, S., Maycock, A., Raddatz, T., Schmidt, H., Toohey, M., Wu, C.-J., Claussen, M., 2020. Global temperature modes shed light on the Holocene temperature conundrum. Nat. Commun. 11, 4726. https://doi.org/10.1038/s41467-41020-18478-41466.

Berger, A., Loutre, M.-F., 1991. Insolation values for the climate of the last 10 million years. Quat. Sci. Rev. 10, 297–317. https://doi.org/10.1016/0277-3791(1091)90033-Q.

Bova, S., Rosenthal, Y., Liu, Z., Godad, S.P., Yan, M., 2021. Seasonal origin of the thermal maxima at the Holocene and the last interglacial. Nature 589, 548–553. https://doi.org/10.1038/s41586-41020-03155-x.

Cartapanis, O., Jonkers, L., Moffa-Sanchez, P., Jaccard, S.L., de Vernal, A., 2022. Complex spatio-temporal structure of the Holocene thermal Maximum. Nat. Commun. 13, 5662. https://doi.org/10.1038/s41467-41022-33362-41461.

Chen, F., Xu, Q., Chen, J., Birks, H.J.B., Liu, J., Zhang, S., Jin, L., An, C., Telford, R.J., Cao, X., Wang, Z., Zhang, X., Selvaraj, K., Lu, H., Li, Y., Zheng, Z., Wang, H., Zhou, A., Dong, G., Zhang, J., Huang, X., Bloemendal, J., Rao, Z., 2015. East Asian summer monsoon precipitation variability since the last deglaciation. Sci. Rep. 5, 11186. https://doi.org/10.11038/srep11186.

Chen, F., Huang, L., Cao, D., Chen, J., Chen, S., Ma, S., Zhou, T., 2024. "Mega-sandwich pattern" of interdecadal precipitation variations and its regional manifestation in the Asian summer precipitation region. Sci. Bull. 69, 2656–2659. https://doi.org/10.1016/j.scib.2024.2606.2026.

Chen, J., Zhang, Q., Huang, W., Lu, Z., Zhang, Z., Chen, F., 2021. Northwestward shift of the northern boundary of the East Asian summer monsoon during the mid-Holocene caused by orbital forcing and vegetation feedbacks. Quat. Sci. Rev. 268, 107136. https://doi.org/10.101016/j.quascirev.102021.107136.

Dansgaard, W., 1964. Stable isotopes in precipitation. Tellus 16, 436–468. https://doi.org/10.3402/tellusa.v3416i3404.8993.

Dee, S.G., Russell, J.M., Morrill, C., Chen, Z., Neary, A., 2018. PRYSM v2. 0: a proxy system model for lacustrine archives. Paleoceanogr. Paleoclimatol. 33, 1250–1269. https://doi.org/10.1029/2018PA003413.

Engstrom, D.R., Nelson, S.R., 1991. Paleosalinity from trace metals in fossil ostracodes compared with observational records at Devils Lake, North Dakota, USA. Palaeogeogr. Palaeoclimatol. Palaeoecol. 83, 295–312. https://doi.org/10.1016/0031-0182(1091)90057-X.

Erb, M.P., McKay, N.P., Steiger, N., Dee, S., Hancock, C., Ivanovic, R.F., Gregoire, L.J., Valdes, P., 2022. Reconstructing Holocene temperatures in time and space using paleoclimate data assimilation. Clim. Past 18, 2599–2629. https://doi.org/10.5194/cp-2518-2599-2022.

Evans, M.N., Tolwinski-Ward, S.E., Thompson, D.M., Anchukaitis, K.J., 2013. Applications of proxy system modeling in high resolution paleoclimatology. Quat. Sci. Rev. 76, 16–28. https://doi.org/10.1016/j.quascirev.2013.1005.1024.

François, L., Goddéris, Y., 1998. Isotopic constraints on the Cenozoic evolution of the carbon cycle. Chem. Geol. 145, 177–212. https://doi.org/10.1016/S0009-2541(1097)00143-00145.

Goddéris, Y., François, L., 1996. Balancing the Cenozoic carbon and alkalinity cycles: Constraints from isotopic records. Geophys. Res. Lett. 23, 3743–3746. https://doi.org/10.1029/3796GL03575.

Goldsmith, Y., Xu, H., Torfstein, A., Lan, J., Song, Y., Zhang, J., Zhou, K.E., Cheng, J., Enzel, Y., 2022. Abrupt contraction of the Indo-East Asian monsoons ended the Holocene humid period. Geophys. Res. Lett. 49, e2022GL100137. https://doi.org/10.101029/102022GL100137.

Guiot, J., Torre, F., Jolly, D., Peyron, O., Boreux, J., Cheddadi, R., 2000. Inverse vegetation modeling by Monte Carlo sampling to reconstruct palaeoclimates under changed precipitation seasonality and $CO_2$ conditions: application to glacial climate in Mediterranean region. Ecol. Model. 127, 119–140. https://doi.org/10.1016/S0304-3800(1099)00219-00217.

Guiot, J., Wu, H., Garreta, V., Hatté, C., Magny, M., 2009. A few prospective ideas on climate reconstruction: from a statistical single proxy approach towards a multi-proxy and dynamical approach. Clim. Past 5, 571–583. https://doi.org/10.5194/cp-5195-5571-2009.

Han, Z., Jia, K., Sun, B., Zhao, S., Li, G., Wu, Q., 2018. Component characteristics and sources of ions in surface water and groundwater of Hulun Lake Basin. Ecol. Environ. Sci. 27, 744–751.

He, F., Clark, P.U., 2022. Freshwater forcing of the Atlantic Meridional Overturning Circulation revisited. Nat. Clim. Chang. 12, 449–454. https://doi.org/10.1038/s41558-41022-01328-41552.

Herzschuh, U., Cao, X., Laepple, T., Dallmeyer, A., Telford, R.J., Ni, J., Chen, F., Kong, Z., Liu, G., Liu, K.-B., 2019. Position and orientation of the westerly jet determined Holocene rainfall patterns in China. Nat. Commun. 10, 2376. https://doi.org/10.1038/s41467-41019-09866-41468.

Hopcroft, P.O., Valdes, P.J., Shuman, B.N., Toohey, M., Sigl, M., 2023. Relative importance of forcings and feedbacks in the Holocene temperature conundrum. Quat. Sci. Rev. 319, 108322. https://doi.org/10.101016/j.quascirev.102023.108322.

Horita, J., Wesolowski, D.J., 1994. Liquid-vapor fractionation of oxygen and hydrogen isotopes of water from the freezing to the critical temperature. Geochim. Cosmochim. Acta 58, 3425–3437. https://doi.org/10.1016/0016-7037(3494)90096-90095.

Ibarra, D.E., Chamberlain, C.P., 2015. Quantifying closed-basin lake temperature and hydrology by inversion of oxygen isotope and trace element paleoclimate records. Am. J. Sci. 315, 781–808. https://doi.org/10.2475/2409.2015.2401.

Jiang, M., Han, Z., Li, X., Wang, Y., Stevens, T., Cheng, J., Lv, C., Zhou, Y., Yang, Q., Xu, Z., 2020. Beach ridges of Dali Lake in Inner Mongolia reveal precipitation variation during the Holocene. J. Quat. Sci. 35, 716–725. https://doi.org/10.1002/jqs.3195.

Jiang, S., Zhou, X., Kok, J.F., Lin, Q., Liu, Y., Zhan, T., Shen, Y., Li, Z., Liu, X., Chen, A., Wang, L., Chen, W., Smol, J.P., Guo, Z., 2024. Enhanced global dust counteracted greenhouse warming during the mid- to late-Holocene. Earth-Sci. Rev. 258, 104937. https://doi.org/10.101016/j.earscirev.102024.104937.

Jiang, W., Guo, Z., Sun, X., Wu, H., Chu, G., Yuan, B., Hatté, C., Guiot, J., 2006. Reconstruction of climate and vegetation changes of Lake Bayanchagan (Inner Mongolia): Holocene variability of the East Asian monsoon. Quatern. Res. 65, 411–420. https://doi.org/10.1016/j.yqres.2005.1010.1007.

Jin, L., Schneider, B., Park, W., Latif, M., Khon, V., Zhang, X., 2014. The spatial–temporal patterns of Asian summer monsoon precipitation in response to Holocene insolation change: a model-data synthesis. Quat. Sci. Rev. 85, 47–62. https://doi.org/10.1016/j.quascirev.2013.1011.1004.

Jin, Z., You, C.-F., Yu, T.-L., Wang, B.-S., 2010. Sources and flux of trace elements in river water collected from the Lake Qinghai catchment, NE Tibetan Plateau. Appl. Geochem. 25, 1536–1546. https://doi.org/10.1016/j.apgeochem.2010.1508.1004.

Jouzel, J., Merlivat, L., 1984. Deuterium and oxygen 18 in precipitation: Modeling of the isotopic effects during snow formation. J. Geophys. Res. Atmos. 89, 11749–11757. https://doi.org/10.11029/JD11089iD11707p11749.

Kaufman, D., McKay, N., Routson, C., Erb, M., Dätwyler, C., Sommer, P.S., Heiri, O., Davis, B., 2020. Holocene global mean surface temperature, a multi-method reconstruction approach. Scientific Data 7, 201. https://doi.org/10.1038/s41597-41020-40530-41597.

Kaufman, D.S., Broadman, E., 2023. Revisiting the Holocene global temperature conundrum. Nature 614, 425–435. https://doi.org/10.1038/s41586-41022-05536-w.

Kim, S.-T., O'Neil, J.R., 1997. Equilibrium and nonequilibrium oxygen isotope effects in synthetic carbonates. Geochim. Cosmochim. Acta 61, 3461–3475. https://doi.org/10.1016/S0016-7037(3497)00169-00165.

Kumke, T., Schölzel, C., Hense, A., 2004. Transfer Functions for Paleoclimate Reconstructions — Theory and Methods. In: Fischer, H., Kumke, T., Lohmann, G., Flöser, G., Miller, H., von Storch, H., Negendank, J.F.W. (Eds.), The Climate in Historical Times: Towards a Synthesis of Holocene Proxy Data and Climate Models. Springer Berlin Heidelberg, Berlin, Heidelberg, pp. 229–243.

Li, G., Wang, Z., Zhao, W., Jin, M., Wang, X., Tao, S., Chen, C., Cao, X., Zhang, Y., Yang, H., 2020. Quantitative precipitation reconstructions from Chagan Nur revealed lag response of East Asian summer monsoon precipitation to summer insolation during the Holocene in arid northern China. Quat. Sci. Rev. 239, 106365. https://doi.org/10.101016/j.quascirev.102020.106365.

Li, Y., Jin, Z., 2013. Seasonal and interannual variations in abundance and oxygen-carbon isotopic compositions of ostracod shells from Lake Qinghai and their controlling factors: a case study on the sediment trap. J. Earth Environ. 4, 1328–1337.

Liang, L., Li, C., Shi, X., Sun, B., Wang, J., Zhou, J., 2017. Characteristics of hydrogen and oxygen isotopes of surface and ground water and the analysis of source of lake water in Hulun Lake Basin, Inner Mongolia. Wetland Sci. 15, 385–390.

Liu, J., Chen, J., Zhang, X., Li, Y., Rao, Z., Chen, F., 2015. Holocene East Asian summer monsoon records in northern China and their inconsistency with Chinese stalagmite $\delta^{18}O$ records. Earth Sci. Rev. 148, 194–208. https://doi.org/10.1016/j.earscirev.2015.1006.1004.

Liu, Z., Zhu, J., Rosenthal, Y., Zhang, X., Otto-Bliesner, B.L., Timmermann, A., Smith, R. S., Lohmann, G., Zheng, W., Elison Timm, O., 2014. The Holocene temperature conundrum, 111, pp. E3501–E3505. https://doi.org/10.1073/pnas.1407229111.

Lu, F., Pausata, F.S., Mohtadi, M., 2024. Reconstruct the intertropical convergence zone over the Indo-Pacific warm Pool with extended records and empirical orthogonal function. Proc. Natl. Acad. Sci. 121, e2408502121. https://doi.org/10.2408501073/pnas.2408502121.

Lunt, D.J., Otto-Bliesner, B.L., Brierley, C., Haywood, A., Inglis, G.N., Izumi, K., Kageyama, M., Kaufman, D., Mauritsen, T., McClymont, E.L., 2024. Paleoclimate data provide constraints on climate models' large-scale response to past CO2 changes. Commun. Earth Environ. 5, 419. https://doi.org/10.1038/s43247-43024-01531-43243.

Ma, F., Chen, J., Chen, J., Wang, T., 2022. Hydrogeochemical and isotopic evidences of unique groundwater recharge patterns in the Mongolian Plateau. Hydrol. Process. 36, e14554. https://doi.org/10.11002/hyp.14554.

Marcott, S.A., Shakun, J.D., Clark, P.U., Mix, A.C., 2013. A reconstruction of regional and global temperature for the past 11,300 years. Science 339, 1198–1201. https://doi.org/10.1126/science.1228026.

Marsicek, J., Shuman, B.N., Bartlein, P.J., Shafer, S.L., Brewer, S., 2018. Reconciling divergent trends and millennial variations in Holocene temperatures. Nature 554, 92–96. https://doi.org/10.1038/nature25464.

Nagashima, K., Tada, R., Toyoda, S., 2013. Westerly jet-East Asian summer monsoon connection during the Holocene. Geochem. Geophys. Geosyst. 14, 5041–5053. https://doi.org/10.1002/2013GC004931.

Osman, M.B., Tierney, J.E., Zhu, J., Tardif, R., Hakim, G.J., King, J., Poulsen, C.J., 2021. Globally resolved surface temperatures since the last Glacial Maximum. Nature 599, 239–244. https://doi.org/10.1038/s41586-41021-03984-41584.

Peltier, W.R., Argus, D., Drummond, R., 2015. Space geodesy constrains ICE age terminal deglaciation: the global ICE-6G_C (VM5a) model. J. Geophys. Res. Solid Earth 120, 450–487. https://doi.org/10.1002/2014JB011176.

Pfahl, S., Wernli, H., 2009. Lagrangian simulations of stable isotopes in water vapor: An evaluation of nonequilibrium fractionation in the Craig-Gordon model. J. Geophys. Res. Atmos. 114, D20108. https://doi.org/10.21029/22009JD012054.

Pfister, C., 2010. The vulnerability of past societies to climatic variation: a new focus for historical climatology in the twenty-first century. Clim. Change 100, 25–31. https://doi.org/10.1007/s10584-10010-19829-10582.

Renssen, H., Seppä, H., Heiri, O., Roche, D.M., Goosse, H., Fichefet, T., 2009. The spatial and temporal complexity of the Holocene thermal maximum. Nat. Geosci. 2, 411–414. https://doi.org/10.1038/ngeo1513.

Rozanski, K., Araguás-Araguás, L., Gonfiantini, R., 1993. Isotopic patterns in modern global precipitation. In: Swart, P.K., Lohmann, K.C., McKenzie, J., Savin, S. (Eds.), Geophysical Monograph 78. American Geophysical Union, pp. 1–36.

Shi, J., Zhou, F., Ma, Q., 2024. Simulation of the changing insolation-precipitation relationship over East Asia during the Holocene. J. Geophys. Res. Atmos. 129, e2024JD041522. https://doi.org/10.041029/042024JD041522.

Thompson, A.J., Zhu, J., Poulsen, C.J., Tierney, J.E., Skinner, C.B., 2022. Northern Hemisphere vegetation change drives a Holocene thermal maximum. Sci. Adv. 8, eabj6535. https://doi.org/10.1126/sciadv.abj6535.

Tierney, J.E., Poulsen, C.J., Montañez, I.P., Bhattacharya, T., Feng, R., Ford, H.L., Hönisch, B., Inglis, G.N., Petersen, S.V., Sagoo, N., Tabor, C.R., Thirumalai, K., Zhu, J., Burls, N.J., Foster, G.L., Goddéris, Y., Huber, B.T., Ivany, L.C., Kirtland Turner, S., Lunt, D.J., McElwain, J.C., Mills, B.J.W., Otto-Bliesner, B.L., Ridgwell, A., Zhang, Y.G., 2020. Past climates inform our future. Science 370, eaay3701. https://doi.org/10.1126/science.aay3701.

Tingley, M.P., Craigmile, P.F., Haran, M., Li, B., Mannshardt, E., Rajaratnam, B., 2012. Piecing together the past: statistical insights into paleoclimatic reconstructions. Quat. Sci. Rev. 35, 1–22. https://doi.org/10.1016/j.quascirev.2012.1001.1012.

Wu, Y., Shi, X., Zhao, S., Lin, T., Ma, J., 2015. Major ion chemistry and influencing factors of three typical lakes in Inner Mongolia Plateau. Ecol. Environ. Sci. 24, 1202–1208.

Xu, Q., Xiao, J., Li, Y., Tian, F., Nakagawa, T., 2010. Pollen-based quantitative reconstruction of Holocene climate changes in the Daihai Lake area, Inner Mongolia, China. J. Climate 23, 2856–2868. https://doi.org/10.1175/2009JCLI3155.2851.

Xu, Z.J., Jiang, F.Y., Zhao, H.W., Zhang, Z.B., Sun, L., 1989. Annals of Hulun Lake. Jilin Literature and History Publishing House, Changchun.

Yu, S.-Y., 2013. Quantitative reconstruction of mid-to late-Holocene climate in NE China from peat cellulose stable oxygen and carbon isotope records and mechanistic models. The Holocene 23, 1507–1516. https://doi.org/10.1177/0959683613496292.

Yu, S.-Y., Kang, Z., Zhou, W., 2012. Quantitative palaeoclimate reconstruction as an inverse problem: a Bayesian inference of late-Holocene climate on the eastern

Tibetan Plateau from a peat cellulose $\delta^{18}O$ record. The Holocene 22, 405–412. https://doi.org/10.1177/0959683611425544.

Zhai, D., Xiao, J., Zhou, L., Wen, R., Chang, Z., Wang, X., Jin, X., Pang, Q., Itoh, S., 2011. Holocene East Asian monsoon variation inferred from species assemblage and shell chemistry of the ostracodes from Hulun Lake, Inner Mongolia. Quatern. Res. 75, 512–522. https://doi.org/10.1016/j.yqres.2011.1002.1008.

Zhang, E., Shen, J., Wang, S., Yin, Y., Zhu, Y., Xia, W., 2004. Quantitative reconstruction of the paleosalinity at Qinghai Lake in the past 900 years. Chin. Sci. Bull. 49, 730–734. https://doi.org/10.1007/BF03184273.

Zhang, W., Wu, H., Cheng, J., Geng, J., Li, Q., Sun, Y., Yu, Y., Lu, H., Guo, Z., 2022. Holocene seasonal temperature evolution and spatial variability over the Northern Hemisphere landmass. Nat. Commun. 13, 5334. https://doi.org/10.1038/s41467-41022-33107-41460.

Zhao, Y., Yu, Z., 2012. Vegetation response to Holocene climate change in East Asian monsoon-margin region. Earth-Sci. Rev. 113, 1–10. https://doi.org/10.1016/j.earscirev.2012.1003.1001.